LAWRENCE
LIVERMORE
NATIONAL
LABORATORY

UCRL-JRNL-226763

POWDER METALLURGY TiAl ALLOYS: MICROSTRUCTURES AND PROPERTIES

L. Hsiung

December 12, 2006

Resent Research Development in Materials Science

Disclaimer

UCRL-JRNL-226763

Recent Research Developments in Materials Science

POWDER METALLURGY TiAl ALLOYS: MICROSTRUCTURES AND PROPERTIES

L. M. Hsiung

University of California
Lawrence Livermore National Laboratory
Materials Science and Technology Division
L-352, P.O. Box 808
Livermore, CA 94551-9900, U.S.A.

ABSTRACT

The microstructures and properties of powder metallurgy TiAl alloys fabricated by hot extrusion of gas-atomized powder at different elevated temperatures were investigated. Microstructure of the alloy fabricated at 1150 °C consisted of a mixture of fine ($\gamma+\alpha_2$) equiaxed grains and coarse ordered B2 grains. Particles of ordered hexagonal ω phase were also observed in some B2 grains. The alloy containing B2 grains displayed a low-temperature superplastic behavior: a tensile elongation of 310% was measured when the alloy was tested at 800 °C under a strain rate of 2×10^{-5} s^{-1}. Microstructure of the alloy fabricated at 1250 °C consisted of a mixture of fine ($\gamma+\alpha_2$) equiaxed grains, coarse α_2 grains, and lamellar ($\gamma+\alpha_2$) colonies. An observation of stacking faults associated with fine γ lamellae in α_2 grains reveals that the stacking fault of α_2 phase plays an important role in the formation of lamellar ($\gamma+\alpha_2$) colonies. Unlike the alloy fabricated at 1150 °, the alloy fabricated at 1250 ° displayed no low-temperature superplasticity, but a tensile elongation of 260% at 1000 °C was measured. Microstructure of the alloy fabricated at 1400 °C consisted of fully lamellar ($\gamma+\alpha_2$) colonies with the colony size ranging between 50 μm and 100 μm, in which the width of γ lamella is in a range between 100 nm and 350 nm, and the width of α_2 lamella is in a range between 10 nm and 50 nm. Creep behavior of the ultrafine lamellar alloy and the effects of alloying addition on the creep resistance of the fully lamellar alloy are also investigated.

INTRODUCTION

TiAl-base aluminide alloys are appealing for use in high-temperature structural applications because of their low density (ρ = 3.9 g/cc), high specific modulus, adequate oxidation resistance, and good strength retention at elevated-temperatures. However, the inherent poor ductility of titanium aluminides at ambient temperatures limits their applications. Material processing and alloy development to improve the low-temperature ductility while retaining their strength especially at elevated temperatures have become the major challenge for the future of the alloys [1, 2]. The poor low–temperature ductility causes conventional manufacturing operations such as rolling, forging, drawing, or machining to be difficult for titanium aluminides. Thus, the development of superplastic TiAl to produce near-net-shape structural components is technologically attractive. To balance low-temperature ductility, fracture toughness, and high-

temperature mechanical properties of TiAl alloys, recent technological developments for the alloys have focused on refining microstructures of the alloys through advanced processing routes such as powder metallurgy processes [3]. A superplastic deformation behavior was recently reported for a PM-TiAl alloy containing metastable B2 phase in association with a fine-grained ($\gamma+\alpha_2$) duplex microstructure [4]. In addition, since both room-temperature and elevated-temperature mechanical properties of PM-TiAl alloys with a fully lamellar microstructure were demonstrated to be superior to those TiAl alloys fabricated by conventional processing techniques such as ingot metallurgy [5-7], there is great interest to further refine lamellar spacing of the alloys to submicron or nanometer length-scales to develop TiAl nanophase composites for engineering applications. A recent report of the formation of nanoscale lamellae (with lamellar spacing in the order of 5 to 10 nm) in a water-quenched TiAl alloy [8] revealed the feasibility of materializing the idea of fabricating TiAl nanophase composites. However, in parallel to make an effort to develop TiAl nanophase composites, there is also a need to understand if further refinement of the lamellar microstructures could lead to adverse effects on high-temperature mechanical properties.

An earlier study on the creep behavior of a Ti-47Al-2Cr-2Nb (at.%) alloy with an ultrafine lamellar microstructure revealed that there existed two distinct creep regimes, where a nearly linear creep behavior [i.e. $\dot{\varepsilon}$ (steady-state creep rate) = $k\sigma^n$, where σ is applied creep stress] was observed in low-stress (**LS**) regime (i.e. $\sigma < 300$ MPa at 760°C), and power-law break down was observed in high-stress (**HS**) regime (i.e. $\sigma > 300$ MPa at 760°C) [9]. Result of a TEM investigation of deformation substructures in creep-deformed specimens revealed the occurrence of interface sliding in **LS** regime and deformation twinning in the **HS** regime, which led us to conclude that the interface sliding associated with viscous glide of pre-existing interfacial dislocations is the predominant creep mechanism in the **LS** regime, and the interface-enhanced deformation twinning in γ lamellae is the predominant creep mechanism in the **HS** regime [10, 11]. Furthermore, it is suggested that the solute atoms segregated at lamellar interfaces may act as short-range barriers to drag the motion of interfacial dislocation arrays during interface sliding. It is also anticipated that more effective barriers to impede the interface sliding can be obtained by interfacial precipitation resulting from the solute segregation. Accordingly, this investigation is extended to the effects of alloying modification on the creep properties of ultrafine lamellar TiAl.

EXPERIMENTAL

TiAl alloys with nominal compositions of Ti-47Al-2Cr-2Nb, Ti-47Al-2Cr-1Nb-1Ta, and Ti-47Al-2Cr-1Nb-0.8Ta-0.2W-B (at.%) were selected for the current investigation. The alloys were fabricated at Oak Ridge National Laboratory by a powder metallurgy process, which involves a hot-extrusion (16:1 ratio) of gas-atomized titanium aluminide powder (particle size: -200 mesh) canned in molybdenum billets. The extrusion processes were carried out at three different temperatures, 1150 °C (T_1), 1250 °C (T_2) and 1400 °C (T_3), which are projected on a Ti-Al pseudo-binary phase diagram shown in Fig. 1. After extrusion, the alloys were annealed at 900 °C for stress relief in a vacuum (~10^{-4} Pa) for 2 h. The phase contents of as-prepared powder and as-fabricated alloys were examined by x-ray diffraction (XRD) using Cu K_α radiation (λ = 0.1546 nm). The detailed microstructures developed from different extrusion temperatures were subsequently examined using transmission electron microscopy (TEM). TEM foils were prepared by a standard twinjet electropolishing technique in an electrolyte of 60%

methanol, 35% butyl alcohol, and 5% perchloric acid at ~15 V and -30 °C. Test specimens with a gauge dimension of 24.4 x 5.08 x 1.52 mm were fabricated from the annealed materials by electrical discharge machining (EDM). To investigate the ductility of the alloys containing duplex microstructures but with different phase content and grain size, tensile tests were conducted on specimens prepared from Ti-47Al-2Cr-1Nb-1Ta alloy extruded at 1150 °C (T_1), and 1250 °C (T_2). Tensile tests were conducted at temperatures ranging between 650 °C and 1100 °C, and at strain rates between 10^{-6} and 10^{-4} s^{-1}. Creep resistance was investigated for alloys extruded at 1400 °C (T_3), which contain fully lamellar microstructures. Creep tests were performed in air at 760 °C and 815 °C, and with applied stresses ranging between 35 MPa and 750 MPa in a dead-load creep machine with a lever arm ratio of 16:1.

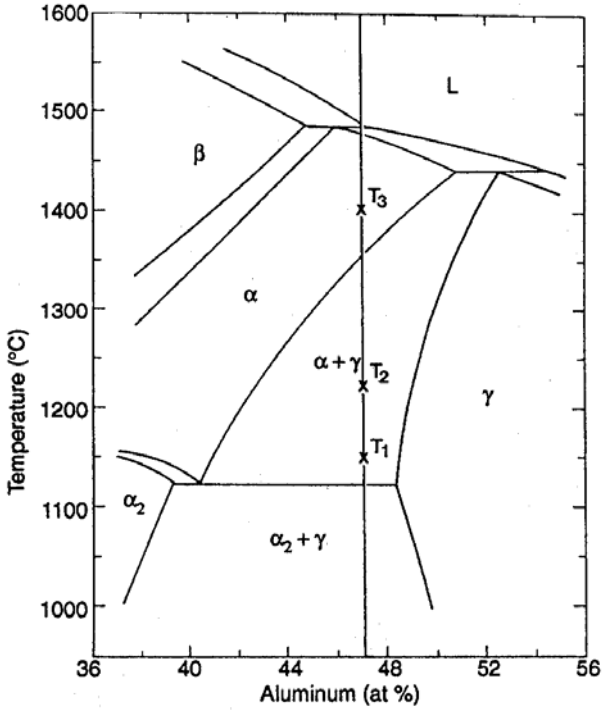

Fig. 1. A pseudo-binary Ti-Al phase diagram showing the extrusion temperatures chosen for the fabrication of powder metallurgy TiAl alloys, T_1: 1150 °C, T_2: 1250 °C and T_3: 1400 °C.

RESULTS AND DISCUSSION

Microstructure of as-prepared TiAl powder

An XRD pattern generated from as-prepared TiAl powder of composition Ti-47Al-2Cr-1Nb-1Ta is shown in Fig. 2. It reveals that the powder contains mainly the α phase ($a \cong 0.29$ nm and $c \cong 0.46$ nm) and some supercooled β ($a \cong 0.323$ nm) phases. It is worth noting that the presence of the β phase in titanium aluminide alloys with alloying additions of β stabilizers such as Cr, Mo, and W has been reported previously [12-14]. It is expected that the addition of Ta and W can further stabilize the β phase at low temperatures. Since the microstructures of as-prepared TiAl powder is not in an equilibrium state, the microstructures of PM alloys are anticipated to be sensitive to the processing history. Accordingly, TEM examinations and analyses were conducted to investigate the microstructures of PM-TiAl alloys fabricated at different extrusion temperatures.

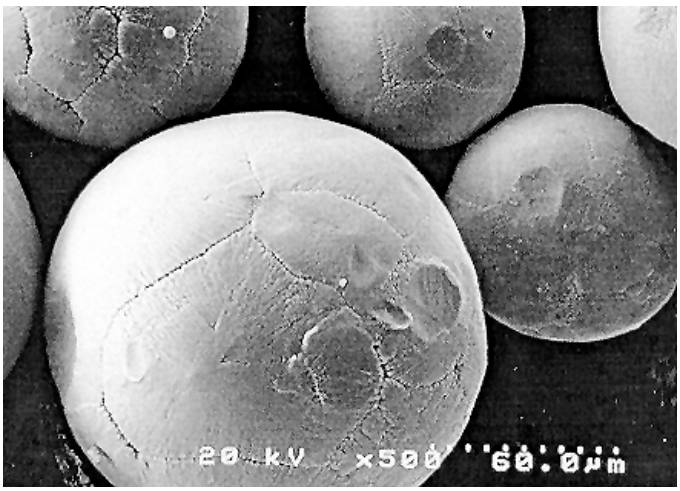

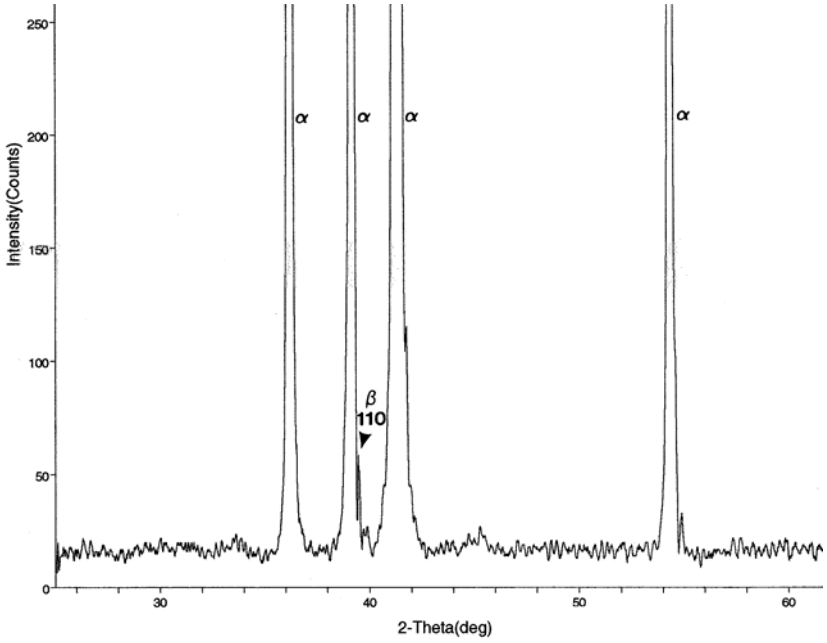

Fig. 2 XRD pattern (Cu K_α) generated from the as-prepared powder sample.

Microstructures of PM-TiAl Alloys

In general, a microstructure consisting of coarse B2 grains and fine ($\gamma+\alpha_2$) grains is obtained in the alloys fabricated at 1150 °C, which is near the eutectoid temperature. A microstructure containing coarse α_2 grains, fine ($\gamma+\alpha_2$) equiaxed grains, and lamellar ($\gamma+\alpha_2$) colonies was formed in the alloys fabricated at 1250 °C, which is in the ($\alpha + \gamma$) phase field. A fully lamellar microstructure was formed within the alloy fabricated at 1400 °C, which is in the α phase field. Here, mainly the microstructures of the Ti-47Al-2Cr-1Nb-1Ta alloy extruded from these three temperatures are reported. The structure-property relationships of the PM-TiAl alloys are demonstrated below.

Microstructure and property of the alloy fabricated at 1150 °C

A typical microstructure of the alloy fabricated at 1150 °C is shown in Fig. 3. A distinct microstructure can be found in the different regions of the micrograph shown in Fig. 3 (a).

According to selected-area diffraction (SAD) analysis, the coarse grains (2 - 5 μm) in the left region have B2 structure, and the fine grains (0.5 - 1 μm) in the right region are mainly a mixture of γ and α_2 grains. That is, whilst some metastable β (or B2) grains are retained in the alloy, a two-phase microstructure composed of equiaxed γ ($L1_0$, TiAl) and α_2 (DO19, Ti_3Al) grains was formed via the $\alpha \rightarrow \gamma + \alpha \rightarrow \gamma + \alpha_2$ transition reactions. In addition, the alloy also contains many elongated grains of B2 phase as shown in Fig. 3 (b). Figure 4 (a) is a dark-field TEM image showing a network of thermal anti-phase boundaries (APBs) observed within a B2 grain, which was imaged by a superlattice reflection ($\boldsymbol{g}$ = 100) under two-beam conditions. The $[001]_{B2}$- and $[111]_{B2}$-zone diffraction patterns of the B2 phase are shown in Fig. 4(b) and 4(c), respectively.

Fine particles of ordered ω phase ($B8_2$, ordered hexagonal) were found to form within B2 grains, and a typical observation of ordered ω particles within a B2 grain [Fig. 5(a)] is shown in Fig. 5. Figure 5(b) is a dark-field image showing the formation of ordered ω particles within a B2 grain shown in Fig. 5(a). The orientation relationships between ordered ω and B2 phases are determined to be $(0001)_\omega \| \{111\}_{B2}$ and $[11\bar{2}0]_\omega \| <1\bar{1}0>_{B2}$ according to the diffraction patterns shown in Fig. 6. The lattice parameters of ordered ω can be derived from that of the parent B2 phase, i.e. $a_\omega = \sqrt{2}\, a_{B2} = 0.457$ nm, and $c_\omega = 3\,(d_{111})_{B2} = 0.559$ nm. It is worth noting that the mechanisms of B2 → ordered ω transitions have been systematically studied in Ti_3Al-Nb alloys [15, 16]. It is accordingly suggested that the ordered ω-lattice in TiAl can be obtained by collapsing one pair of (111) planes within the B2-lattice, and leaving the adjacent (111) planes unaltered as schematically illustrated in Fig. 7.

(a) (b)

Fig. 3. Bright-field TEM images showing typical microstructures of the PM alloy fabricated at 1150 °C. (a) Coexistence of coarse B2 grains with a fine-grained ($\gamma+\alpha_2$) microstructure. (b) Elongated B2 grains.

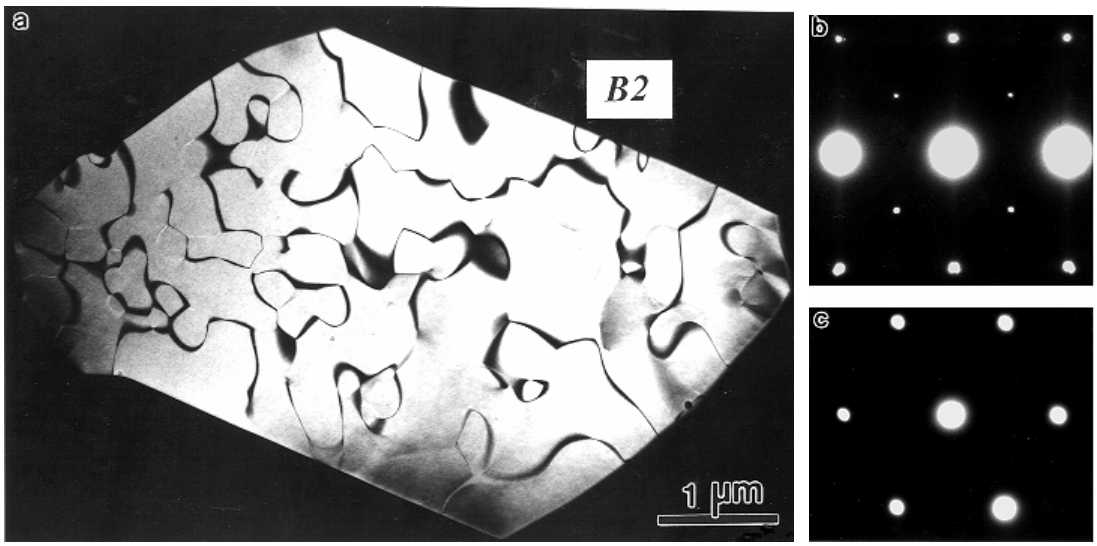

Fig. 4. (a) A dark-field TEM image showing a network of thermal anti-phase boundaries in a B2 grain. (b) SAD pattern of the $[001]_{B2}$-zone, and (c) SAD pattern of the $[111]_{B2}$-zone.

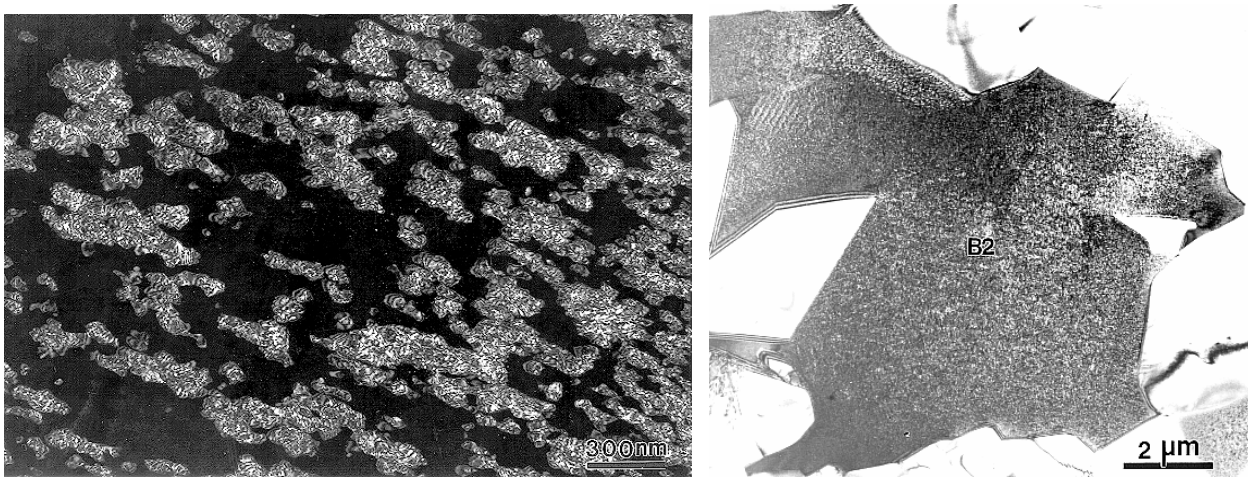

(a) (b)

Fig. 5. (a) A dark-field TEM image showing the formation of ordered ω particles, which were observed from an irregular-shaped B2 grain shown in (b).

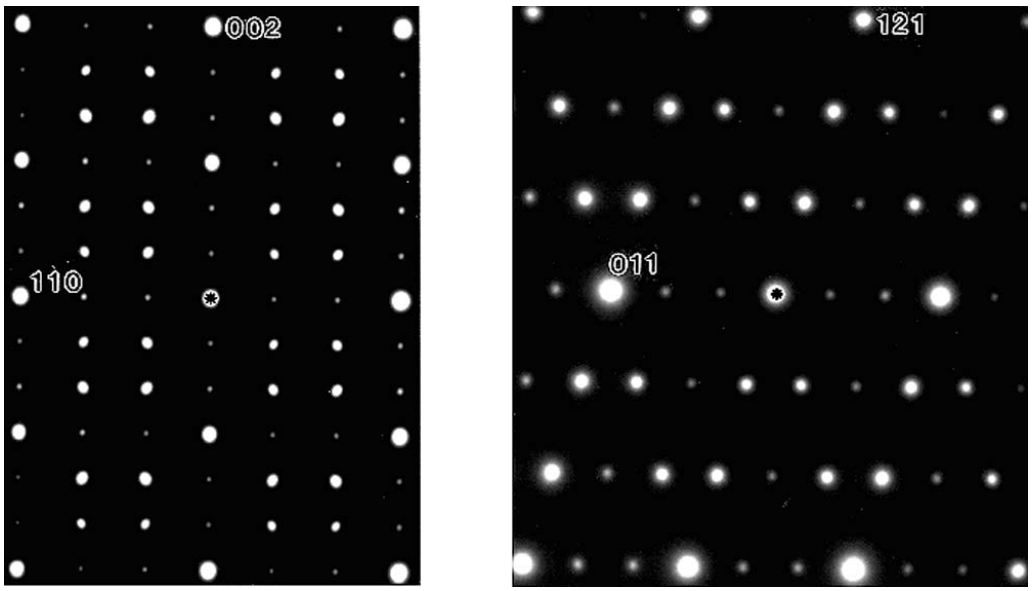

Fig. 6. Diffraction patterns generated from two major zone axes of B2 domain reveal the phase relationships between the B2 and ordered ω phases, (left) $[\bar{2}110]_\omega$ || $<110>_{B2}$, and (right) $[1\bar{2}11]_\omega$||$<311>_{B2}$.

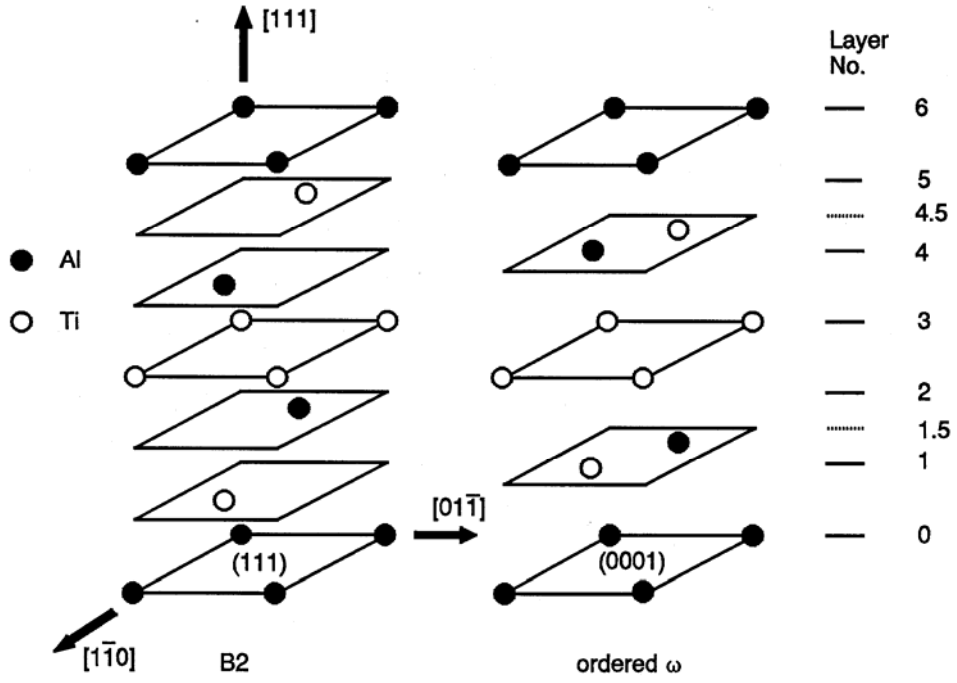

Fig. 7. Lattice correspondence between B2 (ordered bcc) and ordered ω phases based upon the (111)-plane collapse model. The ω-lattice can be obtained by collapsing one pair of (111) planes within B2-lattice.

Results of the alloy samples tensile tested at 800 and 1000 ° C are shown in Fig. 8. The total elongation of both samples over 300% was obtained. Deformation substructure observed from the fractured sample after it was tested at 800 ° C to a 310% elongation is shown in Fig. 9. The

observation of dislocation emission near the triple junction of a grain implies the occurrence of grain boundary sliding during the high-temperature deformation. It is suggested that phase evolution and decomposition of metastable B2 phase into fine grains of γ and α_2 phases during high-temperature deformation could have played a crucial role in the superplastic behavior of the alloy. The decomposition of B2 phase into fine-grains of γ and α_2 phases promotes grain boundary sliding and accommodates the sliding strains to reduce the propensity of cavitation at grain triple junctions and thus delay the fracture process.

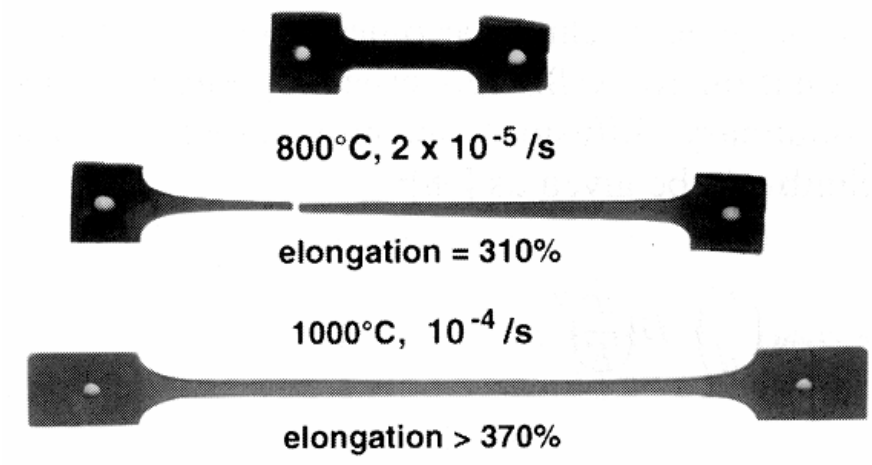

Fig. 8. PM TiAl alloy samples superplastically deformed at 800°C (middle) and 1000°C (bottom). An as-prepared test piece (top) is also shown for comparison.

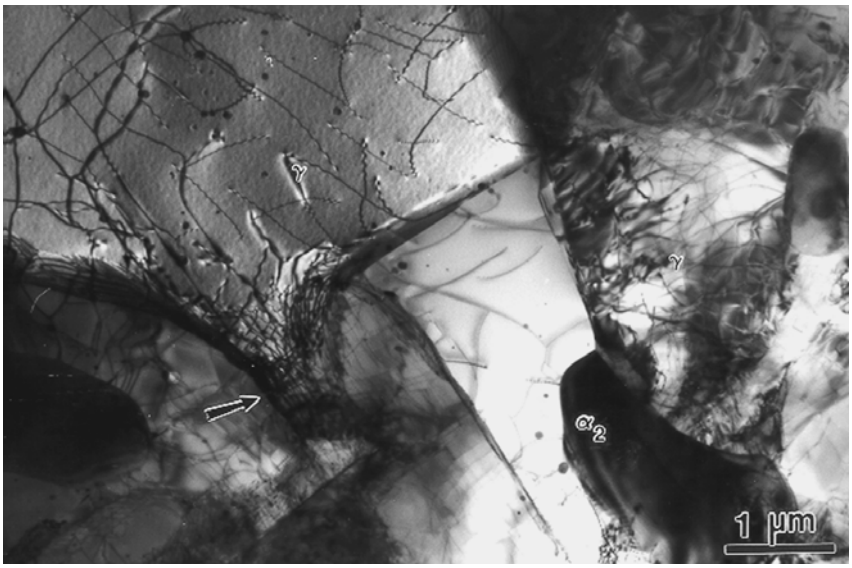

Fig. 9. A coarse two-phase microstructure developed in the sample deformed at 800°C to a fracture (310% elongation). The observation of dislocation emission at a grain-boundary junction (marked by an arrow) suggests that a local stress concentration at junctions might have caused the sample to fracture.

Microstructure and property of the alloy fabricated at 1250°C

A typical microstructure observed in the alloy fabricated at 1250°C is shown in Fig. 10. Similar to that in the alloy extruded at 1150°C, the microstructure contains a two-phase structure of fine γ and α_2 grains [right region of Fig. 10(a)] and coarse α_2 grains [left region of Fig. 10(a)]. Figure 10(b) is a dark-field image showing a network of thermal anti-phase boundaries associated with many planar defects within an α_2-grain. In fact, the planar defects are composed of stacking faults of the α_2 phase and thin plates of the phase. These can be revealed from a TEM analysis shown in Figs. 10(c) and 10(d). Figure 10(c) is a dark-field TEM image showing that some of the defects are actually γ plates (5 ~ 10 nm thick). A twin relationship among these thin γ plates can also be found from the SAD pattern shown in Fig. 10(d). The orientation relationships between γ and α_2 phases are $(111)_\gamma \parallel (0001)_{\alpha 2}$ and $[110]_\gamma \parallel [11\bar{2}0]_{\alpha 2}$. Similar to the hcp → fcc transformation observed in cobalt [17], the stacking faults are intimately related to the formation of the γ plates within the α_2 grains. It is anticipated that if the transformation proceeds further, γ plates would thicken at the expense of the α_2 phase and eventually a lamellar structure composed of γ and α_2 plates could be formed within the parent α_2 grain. It is worth noting that a tensile elongation of 260% at 1000°C was obtained for the alloy, which is inferior to the elongation of the alloy extruded at 1150°C.

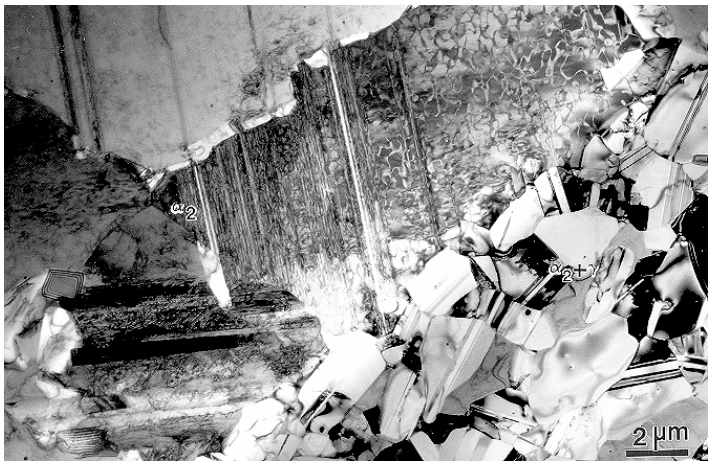

(a)

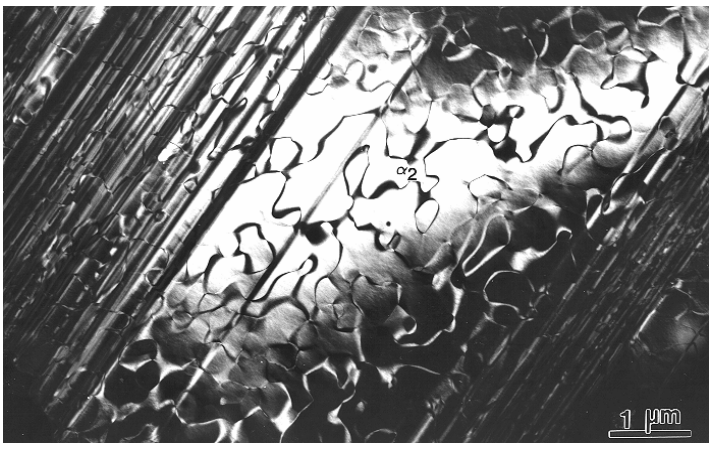

(b)

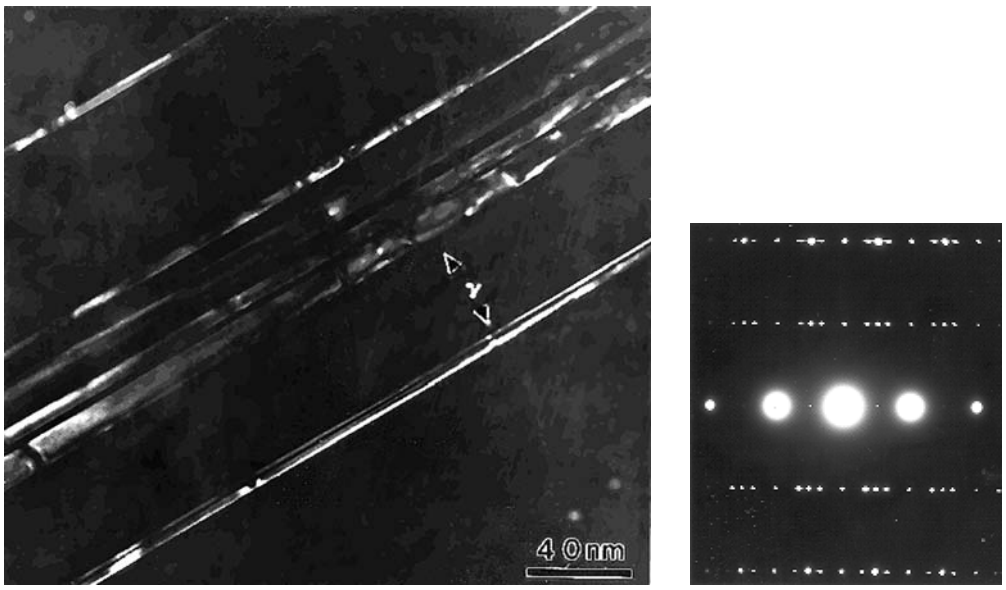

(c) (d)

Fig. 10. (a) A typical microstructure of the alloy fabricated at 1250°C., (b) a dark-field TEM image showing a network of thermal anti-phase boundaries associated with planar defects within an α_2 grain, and (c) a dark-field TEM image revealing that some of the planar defects are γ plates (d) SAD pattern generated from the area in (b), $\mathbf{Z} = [13\bar{2}]_{\gamma}\|[5\bar{4}\bar{1}0]_{\alpha 2}$.

Microstructure and property of the alloy fabricated at 1400°C

A fully lamellar (FL) microstructure (containing γ and α_2 lamellae) is developed in all three alloys (Ti-47Al-2Cr-2Nb, Ti-47Al-2Cr-1Nb-1Ta, and Ti-47Al-2Cr-1Nb-0.8Ta-0.2W-B) hot extruded at 1400°C. Typical lamellar microstructures observed from Ti-47Al-2Cr-2Nb and TiAl-47Al-2Cr-1Nb-0.8Ta-0.2W-B alloys are shown in Figs. 11 (a) and (b). Similar colony sizes (< 100 μm) and lamella widths were observed within these three lamellar alloys. The width of α_2 lamella ranges between 5 nm and 50 nm, and that of γ lamella ranges between 10 nm and 350 nm. These sizes are considerably finer than those in lamellar TiAl alloys fabricated by conventional processing techniques [18]. In addition, as shown in Fig. 11 (c), interwoven-type colony boundaries were formed in these lamellar alloys, which could effectively interlock the colony boundaries from rotation and sliding when deformed at elevated temperatures. In general, there are mainly two types of lamellar interfaces in the lamellar TiAl [19-21]: (1) γ/α_2 interphase interface that has the orientation relationships: $(0001)_{\alpha 2} \parallel (111)_{\gamma}$ and $<11\bar{2}0>_{\alpha 2} \parallel <1\bar{1}0>_{\gamma}$ [which can be determined from the selected-area diffraction (SAD) pattern shown in Fig. 11(a)]; (2) γ/γ interface that includes pseudo-twin and true-twin interfaces. Both pre-existing lattice dislocations (**LD**) in γ lamellae and interfacial dislocations (**ID**) in lamellar interfaces were observed in as-fabricated lamellar TiAl alloys [Fig. 11(d)]. The density of interfacial dislocations in the γ/α_2 interfaces is generally higher than that in the γ/γ interfaces as a result of a greater lattice misfit between γ and α_2 phases. While the interfacial dislocations formed in semi-coherent γ/α_2 interfaces are *1/6*<112> or *1/3*<112> type misfit dislocations [22], those on γ/γ twin-related interfaces are *1/6*$[11\bar{2}]$ type twinning dislocations or geometry necessary

dislocations for accommodating the departure of true-twin interface from the exact (111) twin plane.

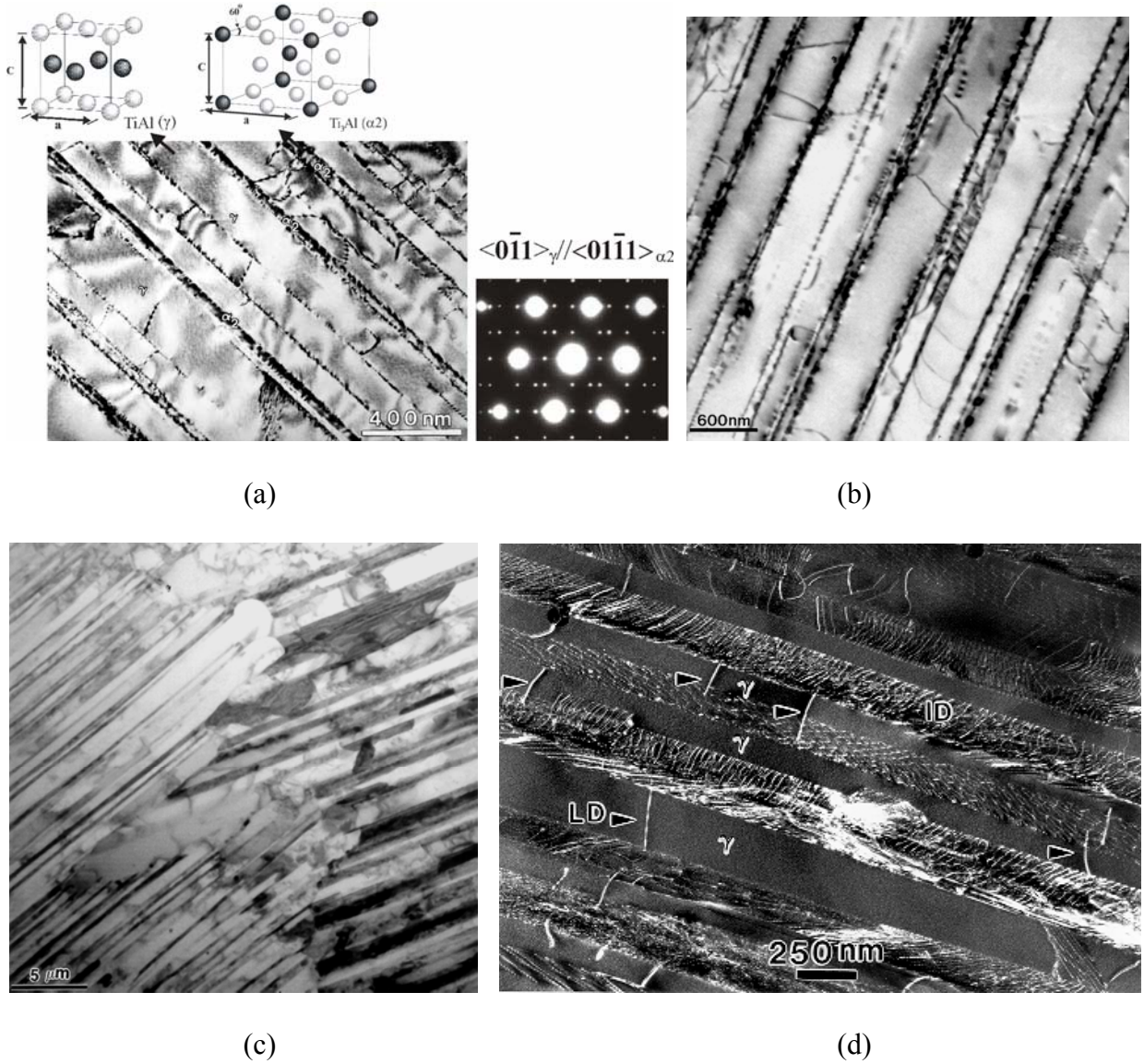

Fig. 11. (a) A bright-field TEM image showing a typical lamellar microstructure observed from Ti-47Al-2Cr-2Nb extruded at 1400°C, and an SAD pattern generated from the domain in (a) showing the phase relationships between γ and α_2, $\mathbf{Z} = [0\bar{1}1]_\gamma \parallel [01\bar{1}0]_{\alpha 2}$; (b) a bright-field TEM image showing a typical lamellar microstructure observed from Ti-47Al-2Cr-1Nb-0.8Ta-0.2W-B extruded at 1400°C; (c) a bright-field TEM image showing a interwoven colony boundary in lamellar Ti-47Al-2Cr-1Nb-0.8Ta-0.2W-B; (d) a tilt view of lamellar microstructure showing a dislocation substructure within the lamellar alloy (**LD** denotes lattice dislocation, and **ID** denotes interfacial dislocation).

Creep data of an ultrafine FL-TiAl (Ti-47Al-2Cr-2Nb) alloy tested at 760°C with a comparison of the creep data of conventional TiAl alloys reported in the open literature is shown in Fig. 12(a) [4]. The refined lamellar alloy demonstrates superior creep resistance among all in the high stress (**HS**) regime and relatively better creep resistance in the low stress (**LS**) regime. Since for engineering applications the structural components are mainly operated in the **LS**

regime, further investigations were conducted to understand the underlying creep mechanism in the **LS** regime in order to improve the creep resistance of the lamellar alloy. By re-plotting the data to correlate the power-law creep (i.e. $\dot{\varepsilon} = k\sigma^n$) as shown in Fig. 12(b), a nearly linear creep behavior ($n \approx 1$, i.e. the steady-sate creep rate is nearly proportional to the applied stress) occurred in the **LS** regime (<300 MPa), and power-law breakdown ($n \approx 7$) took place in *HS* regime (>300MPa). The corresponding deformation substructures observed from specimens deformed under conditions A (138 MPa in **LS** regime) and B (518 MPa in *HS* regime) are shown in Figs. 12(c) and (d), respectively. In general, no significant increase in dislocation density was found within the specimen deformed in the **LS** regime, except that grain boundary ledges presumably formed as a result of interface sliding (caused by the motion of **ID** arrays) are shown in Fig. 12(c). On the other hand, as shown in Fig. 12(d), both the emission of dislocations from lamellar interfaces and the formation of $\{\bar{1}11\}$ <211>-type deformation twins (**DT**) were observed within the specimen deformed in the **HS** regime. The above observations suggest that interface sliding is the predominant deformation mechanism in the **LS** regime, whereas the deformation of γ lamellae by the emission of dislocations and deformation twins from lamellar interfaces becomes the predominant deformation mechanisms in the **HS** regime.

It has been proposed previously [10] that interface sliding associated with a viscous glide of pre-existing interfacial dislocations is the predominant deformation mechanism in lamellar Ti-47Al-2Cr-2Nb creep deformed in the **LS** regime. The interstitial atoms segregated at lamellar interfaces can act as short-range barriers for the motion of interfacial dislocations and resulting in the viscous glide of interfacial dislocations at elevated temperatures. In fact, the high population of interfacial dislocations in lamellar interfaces can act as preferential sites for solute (impurity) segregation, which, for example, the segregation of W solute atoms has recently been identified from a lamellar TiAl-W alloy by Liu et al. using a field-ion atom probe technique [23]. Figure 13 shows a typical observation of a viscous glide (zigzag motion) of interfacial dislocations observed from the specimen deformed in the **LS** regime. The zigzag motion of interfacial dislocations presumably resulted from the locking-unlocking of dislocation lines from solute atoms. Results of in-situ TEM experiments to demonstrate the cooperative motion of interfacial dislocations in lamellar TiAl under room-temperature straining conditions were reported elsewhere [24].. Here, results of in-situ TEM experiments obtained from a creep-deformed sample (138MPa, 760 $^\circ$ C) are presented to demonstrate the motion of interfacial dislocations under an electron-beam heating condition. It is noted that a local heating of the TEM sample can be achieved by spotting the focused electron-beam (several micron meters in size) onto the region of interest in the sample. Figure 14 are two consecutive in-situ images showing the cooperative motion of a dislocation array (total of eight interfacial dislocations in the array) in a γ/γ interface during beam heating, and the array moved about 375 nm after beam heating for 30 seconds. The dislocation array stopped moving after re-spreading the beam onto a wide region of the TEM sample. It is also worthy to note that zigzag motion of the interfacial dislocations were observed, which presumably was caused by the pinning-unpinning of dislocation lines from solute atoms during their movement. These observations support the previously proposed creep mechanism [25]: interface sliding associated with a viscous glide of pre-existing interfacial dislocations is the predominant deformation mechanism for a nearly linear creep behavior observed in the **LS** regime.

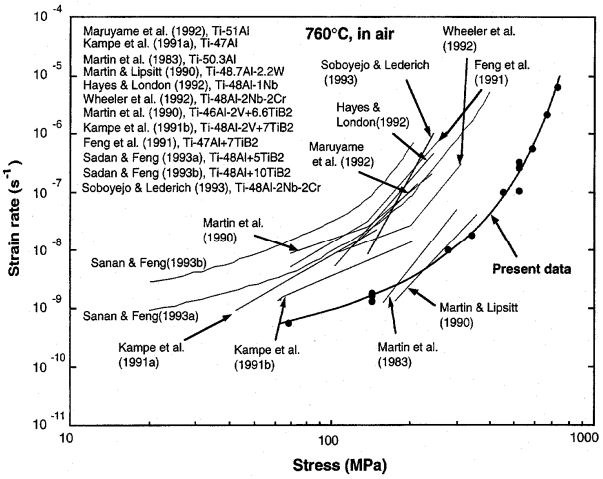
Maruyame et al. (1992), Ti-51Al
Kampe et al. (1991a), Ti-47Al
Martin et al. (1983), Ti-50.3Al
Martin & Lipsitt (1990), Ti-48.7Al-2.2W
Hayes & London (1992), Ti-48Al-1Nb
Wheeler et al. (1992), Ti-48Al-2Nb-2Cr
Martin et al. (1990), Ti-46Al-2V+6.6TiB2
Kampe et al. (1991b), Ti-48Al-2V+7TiB2
Feng et al. (1991), Ti-47Al+7TiB2
Sadan & Feng (1993a), Ti-48Al+5TiB2
Sadan & Feng (1993b), Ti-48Al+10TiB2
Soboyejo & Lederich (1993), Ti-48Al-2Nb-2Cr
760°C, in air
Wheeler et al. (1992)
Soboyejo & Lederich (1993)
Feng et al. (1991)
Hayes & London(1992)
Maruyame et al. (1992)
Martin et al. (1990)
Sanan & Feng(1993b)
Present data
Sanan & Feng(1993a)
Martin & Lipsitt (1990)
Kampe et al. (1991a)
Kampe et al. (1991b)
Martin et al. (1983)
Strain rate (s-1)
Stress (MPa)

(a)

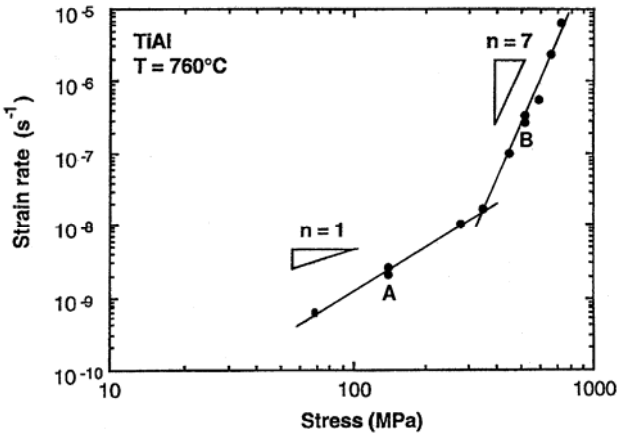
TiAl
T = 760°C
n = 7
n = 1
A
B
Strain rate (s-1)
Stress (MPa)

(b)

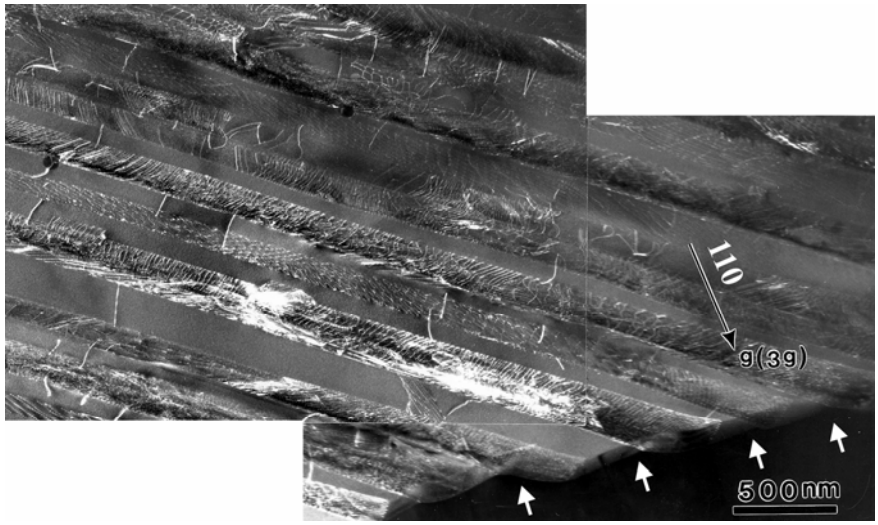
110
g(3g)
500nm

(c)

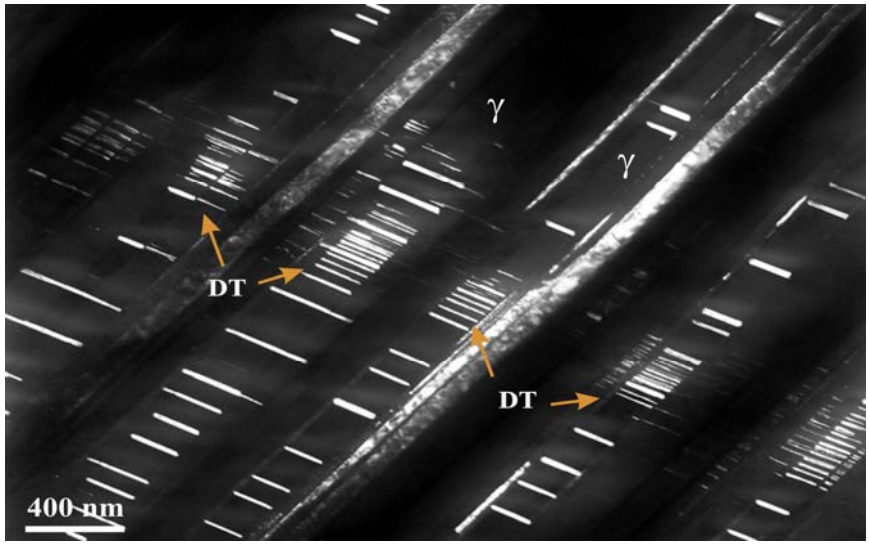
γ
γ
DT
DT
400 nm

(d)

Fig. 12. (a) A comparison of the creep resistance at 760 °C between the presently studied PM alloy and other TiAl alloys [4]; (b) steady-state creep rate plotted as a function of applied stress at 760 °C showing that there existed two distinct creep regimes, i.e. low stress (**LS**) and high stress (**HS**) regimes; (c) a TEM image showing grain boundary ledges (marked by arrows) presumably formed as a result of interface sliding within a specimen creep deformed at 760 °C, 138 MPa, and (d) a weak-beam dark-field TEM image showing the formation of $(\bar{1}\ 11)$ type deformation twins (**DT**) within a specimen creep deformed at 760 °C, 518MPa.

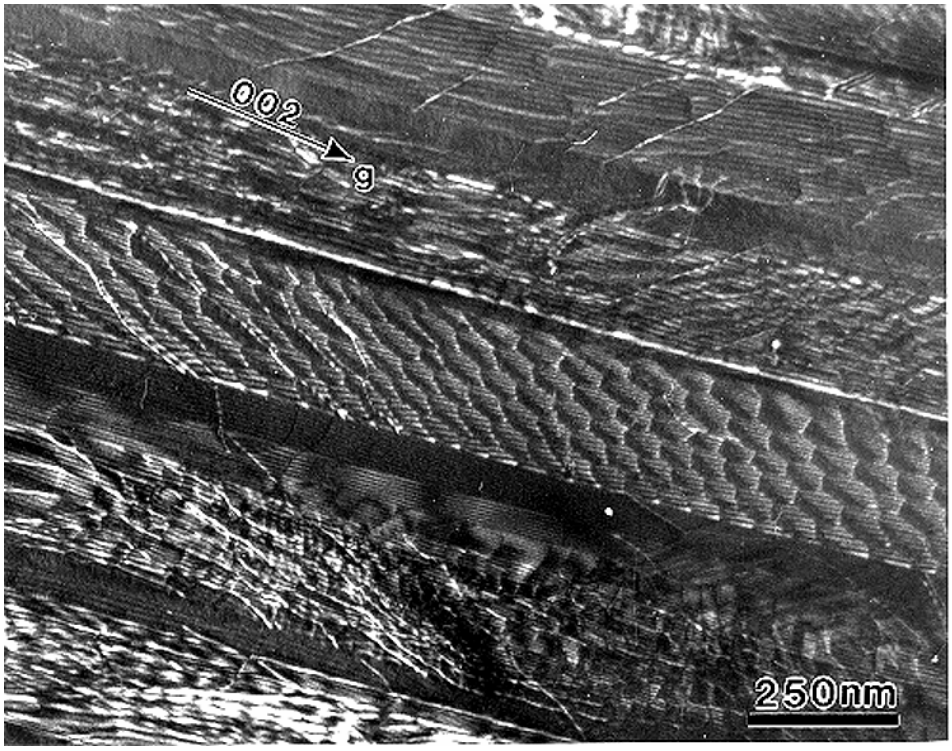

Fig. 13. A weak-beam dark-field TEM image showing the zigzag motion of interfacial dislocation array observed within a specimen creep deformed in the **LS** regime (760 °C, 136 MPa).

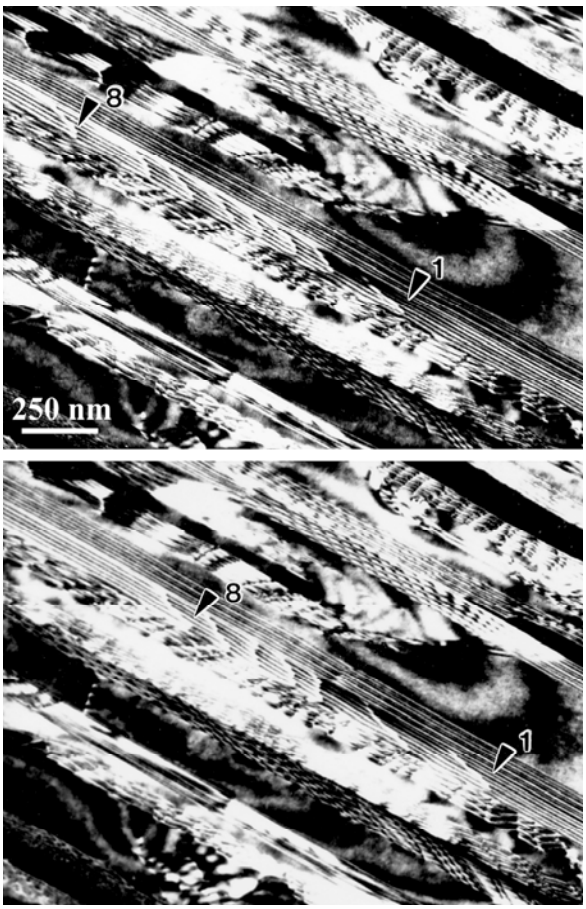

Fig. 14. Two consecutive in-situ TEM images show the cooperative movement of interfacial dislocation (driven by beam heating) in a lamellar interface (time lapse for beam heating: 30 seconds).

It is accordingly suggested that while further refining of lamellar spacing may increase creep resistance of lamellar TiAl in the **HS** regime by restraining **LD** motion within constituent lamellae and impeding **ID** motion by impinging **LD** and **DT** onto lamellar interfaces, it can cause an adverse effect on the creep resistance of lamellar TiAl in the **LS** regime. The creep resistance of refined lamellar TiAl in the **LS** regime may be promoted by reducing the mobility of interfacial dislocations by the segregation of low-diffusivity solutes such as Ta and W to impede the motion of interfacial dislocations. Although more rigorous investigations are needed for the effects of solute segregation at lamellar interfaces on the creep resistance in the **LS** regime, Results demonstrating the promotion of creep resistance of lamellar TiAl by the addition of Ta, W, and B are shown in Figs. 15 and 16(a). As can be seen clearly, both primary and steady state creep rates significantly decrease as a result of the alloying additions, and W solute is anticipated to be more effective than Ta solute for reducing the creep rates. Figure 16(b) shows a result of TEM examination of the Ti-47Al-2Cr-1Nb-0.8Ta-0.2W-0.15B alloy sample creep-deformed at 70 MPa. Here, precipitates, presumably TiB_2-type boride particles, were observed at α_2/γ interfaces. It is noted that the formation of TiB_2-type particles in similar TiAl alloys doped with boron was previously reported elsewhere [26, 27]. It is also noted that no interfacial precipitation was observed at γ/γ interfaces, which suggests that the solute segregation phenomenon is more pronounced at α_2/γ interfaces than at γ/γ interfaces. The above observations indicate that since the activities of glide and climb of lattice dislocations become very limited as a result of a refined lamellar microstructure, creep resistance of refined lamellar TiAl in **LS** regime is mainly controlled by the mobility of interfacial dislocations.

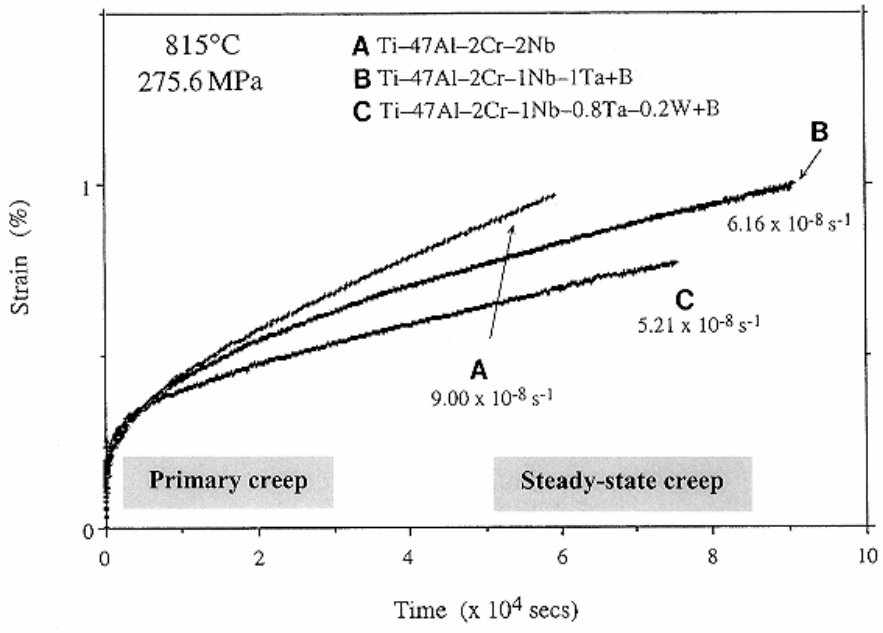

Fig. 15. Creep data showing the effects of W and Ta additions to the creep resistance of PM FL-TiAl alloys at 815 °C. It reveals that W solute is more effective than Ta solute for reducing both primary and steady creep rates.

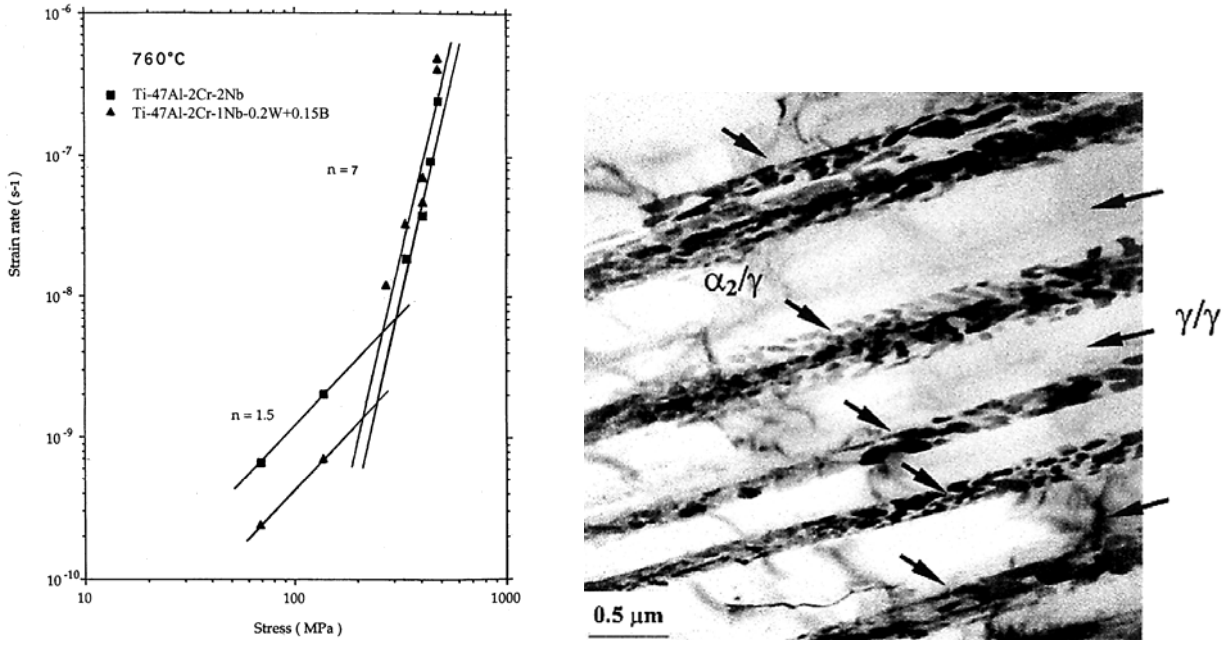

(a) (b)

Fig. 16. (a) Creep data showing the effects of alloying modification to the creep resistance of refined lamellar TiAl alloys in **LS** regime at 760 °C; (b) A bright-field TEM image showing the formation of TiB_2-type boride particles at α_2/γ interfaces within a Ti-47Al-2Cr-1Nb-0.8Ta-0.2W-0.15B alloy sample creep-deformed at 760 °C, 70 MPa. Notice that no precipitation was found in γ/γ interfaces which appeared as faint contrasts in (b).

SUMMARY

The effects of fabrication temperatures on the microstructures of powder metallurgy TiAl alloys were reviewed. The as-prepared TiAl powder consists of mainly metastable α phase and supercooled β/B2 phase. Different microstructures were developed depending on the extrusion temperatures (1150°C, 1250°C, and 1400°C) chosen to fabricate the alloys. The alloy fabricated at 1150°C was found to consist of coarse grains of B2 phase and fine-grains of γ and α_2 phases. Ordered ω particles were also observed within some B2 grains. The orientation relationships between ordered ω and B2 phases are determined to be $(0001)_\omega || \{111\}_{B2}$ and $[11\bar{2}0]_\omega || <1\bar{1}0>_{B2}$, and the lattice parameters of ordered ω are $a_\omega = 0.457$ nm and $c_\omega = 0.559$ nm. This PM-TiAl containing the metastable B2 grains displayed a low-temperature superplastic behavior, in which tensile elongations of 310% and 370% were obtained when tensile-tested at 800°C and 1000°C, respectively. It is suggested that both fine-grained (γ + α_2) microstructure and microstructural evolution resulting from the decomposition of metastable B2 grains play a crucial role in the superplastic deformation of PM-TiAl. Tensile elongation significantly decreases for the PM-TiAl extruded at 1250°C that consists of a similar fine-grained (γ + α_2) microstructure but without B2 grain; an elongation of 260% was obtained for a sample tensile-tested at 1000°C. A refined fully lamellar (FL) microstructure (γ lamellae: 100 ~ 300 nm thick, and α_2 lamellae: 10 ~ 50 nm thick) was formed in the alloy extruded at 1400°C. The creep resistance of refined FL-TiAl alloy is in general superior to that of TiAl alloys fabricated by conventional processing techniques. The creep resistance of ultrafine lamellar TiAl can be improved by the alloying addition of tungsten and boron so as to impede the interface sliding by reducing the mobility of interfacial dislocations.

ACKNOWLEDGEMENTS

This work was performed under the auspices of the U. S. Department of Energy by the University of California, Lawrence Livermore National Laboratory under Contract No. W-7405-Eng-48.

REFERENCES

1. Y-W. Kim and D.M. Dimiduk, 1991, JOM **43**(8), 40.
2. M. Yamaguchi, 1992, Mater. Sci. Technol. **8**, 299.
3. J. N. Wang, A. J. Schwartz, T. G. Nieh, C. T. Liu, V. K. Sikka, and D. Clemens, 1995, in Gamma Titanium Aluminides, ed. Y-W. Kim et al., TMS (Warrendale, PA), 949.
4. T. G. Nieh, L. M. Hsiung, and J. Wadsworth, 1999, Intermetallics **7**, 163.
5. C. T. Liu, P. J. Maziasz, D. R. Clemens, J. H. Schneibel, V. K. Sikka, T. G. Nieh, J. Wright, and L. R. Walker, 1995, in Gamma Titanium Aluminides, ed. Y-W. Kim et al., TMS (Warrendale, PA), 679.
6. C. T. Liu, J.H. Schneibel, P. J. Maziasz, J. L. Wright, and D. S. Easton, 1996, Intermetallics **4**, 429.
7. P. J. Maziasz and C. T. Liu, 1998, Metall. Mater. Trans. A, **29A**, 105.
8. K. Hono, E. Abe, T. Kumagai, and H. Harada, 1996, Scripta Mater. **35**, 495.
9. J. N. Wang and T. G. Nieh, 1998, Acta Mater. **46**, 1887.
10. L. M. Hsiung and T. G. Nieh, 1999, Intermetallics **7**, 821.
11. L. M. Hsiung, T. G. Nieh, B. W. Choi, and J. Wadsworth, 2002, Mater. Sci. Eng. **A329/31**,

637.
12. M. A. Morris, Y. G. Liand, and M. Leboeuf, 1994, Scripta Metall. Mater. **31**, 449.
13. K. Nakai, T. Ono, H. Ohtsubo, and Y. Ohmoni, 1995, *Mater. Sci. Eng*. **192/193A**, 922.
14. N. Masahashi and Y. Mizuhara, 1995, in Gamma Titanium Aluminides, ed. Y-W. Kim et al., TMS (Warrendale, PA), 165.
15. R. Strychor, J. C. Williams, and W. A. Soffa, 1998, Met. Trans. A., **19A**, 225.
16. L. A. Bendersky, W. J. Boettinger, B. P. Burton, and F. S. Biancaniello, 1990, Acta Metall. Mater. **38**, 931.
17. J. A. Graves, L. A. Bendersky, F. S. Biancaniello, J. H. Perepezko, and W. J. Boettinger, 1988, Mater. Sci. Eng. **98**, 265.
18. Y-W. Kim, 1995, Mater. Sci. Eng. **192A**, 519.
19. M. Yamaguchi and Y. Umakoshi, *Progress in Materials Science* **34**, 1 (1990).
20. M. Yamaguchi and H. Inui, 1993, in Structural Internietallics, ed. Darolia, R. et al., TMS (Warrendale, PA), 127.
21. Y. Yamamoto, M. Takeyama, and T. Matsuo, 2002, Mater. Sci. Eng. **A329-331**, 631.
22. L. M. Hsiung and T. G. Nieh, 1997, Mater. Sci. Eng. **A239-240**, 438.
23. C. T. Liu, P. J. Maziasz, and D. J. Larson, 1998, in Interstitial and Substitutional Solute Effects in Intermetallics, ed. Baker et al., TMS (Warrendale, PA), 179.
24. L. M. Hsiung, J. Zhou, and T. G. Nieh, 2006, J. of Mater. Res. **21**, p. 2453.
25. M. De Graef, D.A. Hardwick, and P.L. Martin, 1993, in Structural Intermetallics, ed. M.V. Nathal et al., TMS (Warrendale, PA), 177.
26. D. J. Larson, C. T. Liu, and M. K. Miller, 1997, Intermetallics **5**, 411.
27. C. T. Liu, J. L. Wright, and S. C. Deevi, 2002, Mater. Sci. and Eng. **A329 – 331**, 416.